



HAL
open science

Imaging the crust and uppermost mantle structure of Portugal (West Iberia) with seismic ambient noise

Graça Silveira, Nuno Afonso Dias, Sergey Kiselev, Eleonore Stutzmann, Susana Custódio, Martin Schimmel

► To cite this version:

Graça Silveira, Nuno Afonso Dias, Sergey Kiselev, Eleonore Stutzmann, Susana Custódio, et al.. Imaging the crust and uppermost mantle structure of Portugal (West Iberia) with seismic ambient noise. *Geophysical Journal International*, 2022, 10.1093/gji/ggac106 . insu-03643034

HAL Id: insu-03643034

<https://insu.hal.science/insu-03643034>

Submitted on 16 Mar 2023

HAL is a multi-disciplinary open access archive for the deposit and dissemination of scientific research documents, whether they are published or not. The documents may come from teaching and research institutions in France or abroad, or from public or private research centers.

L'archive ouverte pluridisciplinaire **HAL**, est destinée au dépôt et à la diffusion de documents scientifiques de niveau recherche, publiés ou non, émanant des établissements d'enseignement et de recherche français ou étrangers, des laboratoires publics ou privés.

Imaging the crust and uppermost mantle structure of Portugal (West Iberia) with seismic ambient noise

Graça Silveira^{1,2}, Nuno Afonso Dias^{1,2}, Sergey Kiselev³, Eleonore Stutzmann⁴,
Susana Custódio¹ and Martin Schimmel⁵

¹*Instituto Dom Luiz (IDL), Faculdade de Ciências, Universidade de Lisboa, Campo Grande, 1749–016 Lisboa, Portugal. E-mail: mdsilveira@fc.ul.pt*

²*Instituto Superior de Engenharia de Lisboa, Instituto Politécnico de Lisboa, 1959-007 Lisboa, Portugal*

³*Institute of Physics of the Earth, 10-1, Bolshaya Gruzinskaya str., Moscow 123242, Russia*

⁴*Institut de Physique du Globe de Paris, Université Paris Cité, CNRS, 1 rue Jussieu, 75005 Paris, France*

⁵*Geosciences Barcelona, CSIC, Lluís Sole i Sabaris s/n, E-08028 Barcelona, Spain*

Accepted 2022 March 14. Received 2022 February 23; in original form 2021 September 21

SUMMARY

We present a new high-resolution 3-D shear wave velocity (V_s) model of the crust and uppermost mantle beneath Portugal, inferred from ambient seismic noise tomography. We use broad-band seismic data from a dense temporary deployment covering the entire Portuguese mainland between 2010 and 2012 in the scope of the WILAS project. Vertical component data are processed using phase correlation and phase weighted stack to obtain empirical Green functions (EGFs) for 2016 station pairs. Further, we use a random sampling and subset stacking strategy to measure robust Rayleigh-wave group velocities in the period range 7–30 s and associated uncertainties. The tomographic inversion is performed in two steps: First, we determine group-velocity lateral variations for each period. Next, we invert them at each grid point using a new trans-dimensional inversion scheme to obtain the 3-D shear wave velocity model. The final 3-D model extends from the upper crust (5 km) down to the uppermost mantle (60 km) and has a lateral resolution of ~ 50 km. In the upper and middle crusts, the V_s anomaly pattern matches the tectonic units of the Variscan Massif and Alpine basins. The transition between the Lusitanian Basin and the Ossa Morena Zone is marked by a contrast between moderate- and high-velocity anomalies, in addition to two arched earthquake lineations. Some faults, namely, the Manteigas–Vilariça–Bragança fault and the Porto–Tomar–Ferreira do Alentejo fault, have a clear signature from the upper crust down to the uppermost mantle (60 km). Our 3-D shear wave velocity model offers new insights into the continuation of the main tectonic units at depth and contributes to better understanding the seismicity of Portugal.

Key words: Crustal imaging; Seismic interferometry; Seismic tomography; Surface waves and free oscillations; Crustal structure.

1 INTRODUCTION

The crustal structure of the Iberian Peninsula (*cf.* Fig. 1) is the result of several major geological events of amalgamation and breakup, the most relevant of which are the Variscan Orogeny in the Late Palaeozoic, when the collision of Gondwana and Laurussia formed Pangea (e.g. Matte 1986, 1991, 2001; Ribeiro *et al.* 2007; Arenas *et al.* 2016a), and the Mesozoic extensional tectonic activity that led to the opening of the North Atlantic Ocean (e.g. Ribeiro *et al.* 1990; Pinheiro *et al.* 1996; De Vicente *et al.* 2011; Pereira & Alves 2013; Jeannot *et al.* 2016; Pereira *et al.* 2016).

Portugal, in Western Iberia, comprises several blocks of the Variscan orogen in SW Europe (*cf.* Fig. 1a). Most of Portugal is part the Iberian Massif (*cf.* Fig. 1b), composed of Variscan rocks

with ages ranging 380–280 Myr (Simancas *et al.* 2013; Arenas *et al.* 2016a) and a few outcrops dating back to the Neoproterozoic Cadomian Orogeny (660–540 Myr; Linnemann *et al.* 2008; Ribeiro *et al.* 2009). The subsidence of the western and southern margins of Iberia, in response to the opening of the North Atlantic Ocean, created several basins of deep crustal signature, with rocks dating back to 125–37 Myr, which were later uplifted during the Alpine orogeny (Pereira & Alves 2013; Jeannot *et al.* 2016; Pereira *et al.* 2016).

As a result of this complex geological past, several important tectonic contacts or faults can be observed inland, even though some are partially covered by recent Cenozoic basins. Based on tectonostratigraphic criteria, the Iberian Massif that outcrops in Portugal is usually divided into four main tectonic units. From the

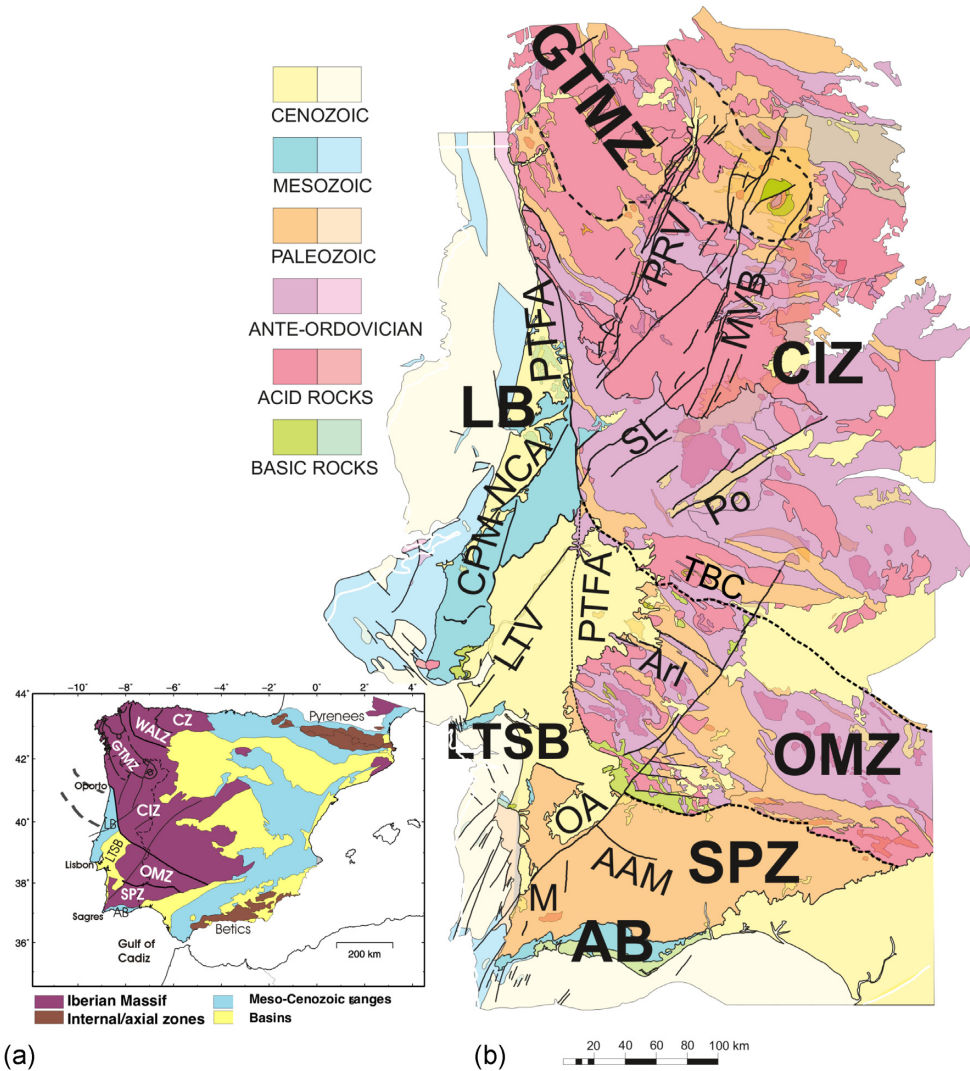


Figure 1. (a) Simplified structural map showing the main tectonic units of the Iberian Peninsula. Iberian Massif: Cantabrian Zone (CZ), West-Asturian-Leonese Zone (WALZ), Galicia-Trás-os-Montes Zone (GTMZ), Central Iberian Zone (CIZ), Ossa Morena Zone (OMZ) and South Portuguese Zone (SPZ). The western and southern limits of the Massif are defined by several basins: Lusitanian Basin (LB), Lower-Tagus and Sado Rivers Basin (LTSB) and Algarve Basin (AB). (b) Simplified geological map of Portugal, showing the inner structure of the Portuguese Iberian Massif and main fault systems (adapted from Veludo *et al.* 2017): Porto-Tomar-Ferreira do Alentejo shear zone (PTFA); Tomar-Badajoz-Córdoba shear zone (TBC); Penacova-Régua-Verin fault system (PRV); Manteigas-Vilariça-Bragança fault system (MVB); Seia-Lousã fault (SL); Ponsul fault (Po); Nazaré-Condeixa-Alvaiázere fault (NCA); Candeeiros-Porto de Mós fault (CPM); Lower-Tagus Valley fault system (LTV); Arraiolos-Ciborro fault (Arl); Odemira-Ávila fault (OA); Albornoa-Aljustrel-Messejana Alignment (AAM); Monchique sienitic intrusion (M).

internal to the external domains of the Ibero-Armorican Arc and from north to south (*cf.* Fig. 1), we have: (1) the Galicia-Trás-os-Montes Zone (GTMZ), which consists of a pile of allochthonous thrust sheets, overlying (2) the autochthonous Central Iberian Zone (CIZ), (3) the para-autochthonous Ossa-Morena Zone (OMZ) and (4) the allochthonous South Portuguese Zone (SPZ).

The western and southern coasts of Iberia are dominated by the Lusitanian Basin (LB) and Algarve (AB), with a deep crustal signature, composed of uplifted Mesozoic rocks and Cenozoic sedimentary sequences (Ribeiro *et al.* 2007; Arenas *et al.* 2016a; Veludo *et al.* 2017), and by the Cenozoic Lower-Tagus and Sado Sedimentary Basin (LTSB).

Some of the faults inherited from the complex tectonic history of western Iberia have been reactivated since the Miocene (*ca.* 20 Myr; Pinheiro *et al.* 1996), in response to the NW–SE Africa–Eurasia convergence (4.5–5.6 mm yr⁻¹; Fernandes *et al.* 2003).

Currently, mainland Portugal displays a medium seismicity rate, with several destructive earthquakes documented in the historical period (Custódio *et al.* 2015).

The first studies that characterized the seismic properties of the crust and upper mantle beneath Portugal, in the 1970–1980s, used controlled sources and provided mainly 1-D or 2-D P -wave velocity (V_p) profiles (Victor *et al.* 1980; Sousa Moreira *et al.* 1983; Téllez *et al.* 1993; Matias 1996; Carbonell *et al.* 2004; Afilhado *et al.* 2008; Díaz & Gallart 2009; Flecha *et al.* 2009; Palomeras *et al.* 2009). Over the last decade, several new studies took advantage of the increasing coverage provided by seismic networks to infer more detailed information. The first work to uniformly cover mainland Portugal was carried out by Silveira *et al.* (2013), who obtained Rayleigh-wave dispersion maps using ambient noise techniques. Although not inverting for V_s structure, the group-velocity maps showed a clear correlation with the major structural units of

western Iberia. Using Ps receiver-functions, Dündar *et al.* (2016) obtained a first image of the average crustal V_p/V_s ratio, together with a Moho topography that also showed some correlation with tectonic units. Veludo *et al.* (2017), using local earthquake tomography, obtained the first 3-D maps of V_p and V_p/V_s beneath Portugal. They achieved a high-resolution imaging for most of the tectonic contacts, but were limited to the upper 20 km of the crust. Atanayake *et al.* (2017), based on Rayleigh-wave ellipticity, built a V_s model of the crust using 33 permanent and temporary stations in Portugal. Their model showed low shear wave speeds in the sedimentary basins and in some sectors of the Central Iberian Zone. Higher seismic velocities were imaged in the Galicia-Trás-os-Montes Zone. Corela *et al.* (2017) computed a regional ambient noise tomographic model integrating seafloor- and land-based data, focusing in the southwest Portuguese margin. Using teleseism body-wave tomography, Civiero *et al.* (2018, 2019) extended the imaging of the region, obtaining P - and S -wave 3-D models from 70 km down to 800 km depth. However, the regional scale analysis of the entire Ibero-Western Maghreb Region resulted in models with only crude details of the structure of the lithosphere beneath Portugal, starting at 70 km depth and extending downward into the mantle.

Despite these different studies at different scales, several questions remain unanswered, namely: What is the relation between the current surface topography and the deep crustal/lithospheric structure? How was it influenced by the past tectonic events, namely the several units composing the W Iberian Terrane, CIZ, OMZ and SPZ? Is the anomalous concentration of seismicity in the interior of the Iberian microplate, namely in northern Alentejo (Arraiolos-Portel), western edge (Estremadura), northern Portugal (Vilariça, Chaves), in some measure due to an inherited structure from past orogenies? If so, how far has past subduction history influences the subduction dynamics observed on the southern margin of Iberia?

In this work, we provide the missing link between previous crustal- and mantle-scale studies, presenting a new upper lithospheric-scale high-resolution 3-D seismic model of Portugal. To this end, we use a state-of-the-art methodology of ambient noise tomography. Empirical Green functions (EGFs) are computed using phase correlation and phase weighted stack (Schimmel *et al.* 2011). Robust group velocities and their uncertainties are measured using the S -transform, combined with a random sampling and subset stacking method. Regionalized group velocities are then inverted on a 2-D grid using a novel trans-dimensional inversion scheme, resulting in a new high-resolution S -wave velocity model of the Portuguese crust and upper mantle down to 60 km. The model has a lateral resolution of 50 km, allowing to investigate the signature at depth of the geological structures observed at the surface.

2 DATA PROCESSING

The data used in this study was recorded continuously during 24 months, from June 2010 to June 2012, by a network of 54 broad-band stations. This network had an average interstation distance of ~ 50 km and was designed in the framework of project WILAS (Dias *et al.* 2010). Data from the DOCTAR experiment (2011–2012) were also included, resulting in a densification of the seismic network in the Alentejo region (Matos *et al.* 2018) and increasing the total number of stations to 64 (Fig. 2). Overall, we used data from networks PM (Instituto Português do Mar e da Atmosfera, I.P. 2006), LX (Instituto Dom Luiz (IDL)-Faculdade De Ciências Da Universidade De Lisboa 2003), WM (San Fernando Royal Naval

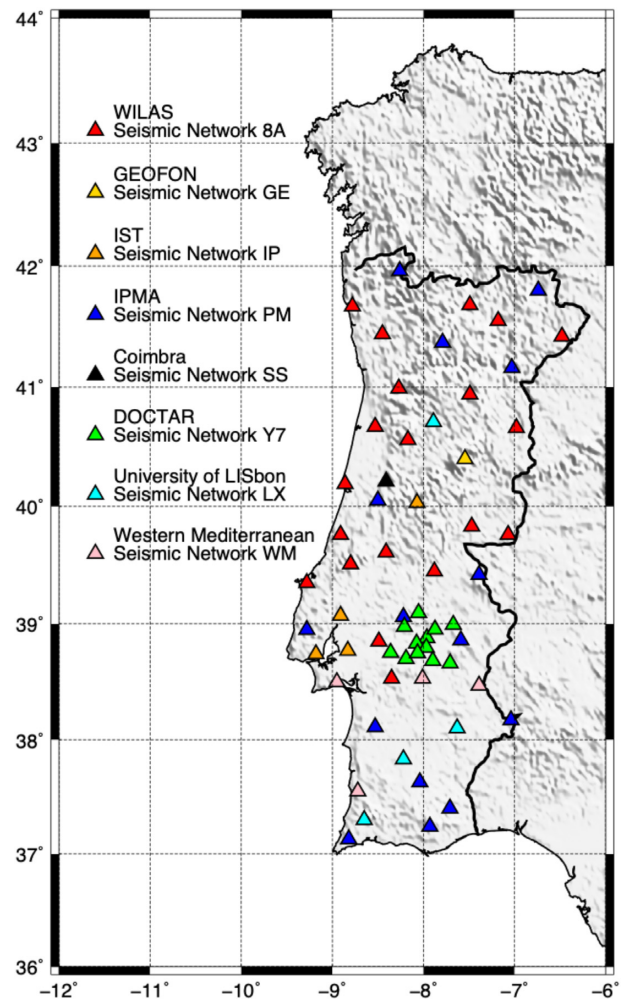


Figure 2. Location of the broad-band seismic stations used in this study. The colours mark the different seismic networks. Temporary networks operated between 2010–2012 (WILAS 8A) and 2011–2012 (DOCTAR Y7).

Observatory (ROA) 1996), IP, GE (GEOFON Data Centre 1993), SS, 8A (Dias *et al.* 2010), Y7.

The 64 seismic stations were equipped with a variety of broad-band seismometers, with corner frequencies ranging from 30 to 120 s (Guralp CMG-40T, Guralp CMG-3T, Guralp CMG-3ESP, Streckeisen STS-2), and several types of data loggers (Earth Data PR6-24, Reftek, Quanterra). Data was recorded continuously at 40, 50, 80 and 100 samples per second. More detailed information on the permanent networks and on the WILAS temporary network (Dias *et al.* 2010) can be found in Carrilho *et al.* (2021) and Custódio *et al.* (2014). The DOCTAR deployment is described in Matos *et al.* (2018).

The estimation of Rayleigh-wave EGFs from ambient noise cross-correlations was made in three main steps: (1) pre-processing; (2) cross-correlation for each interstation pair and (3) stack of correlograms to improve the signal-to-noise ratio. The first step (pre-processing) comprises decimation to one sample per second, instrumental response removal and data conversion to true ground velocity, mean removal and detrending.

We are interested in the period range that includes the primary and secondary microseisms, where ambient noise energy is highest and consists mainly of surface waves. Also, due to the interstation spacing (Supporting Information Fig. S3) and network aperture

(Fig. 2), the optimal period band ranges from 5 to 30 s. Therefore, we apply a fourth-order zero-phase bandpass Butterworth filter in the period range between 2 and 50 s that eliminates energy outside our range of interest. Finally, we divide the entire data set into 24-hr-length time-series.

As shown in previous studies (see for e.g. Bensen *et al.* 2007, 2008; Silveira *et al.* 2013), the use of the classical cross-correlation and linear stack methods requires preliminary time-domain normalization and spectral whitening to reduce the influence of other large-amplitude events such as earthquakes. In this study, we apply the Phase Cross-Correlation method (PCC), followed by a time-frequency Phase-Weighted Stack (tf-PWS), built by Schimmel & Gallart (2007) upon the PWS developed by Schimmel & Paulssen (1997) (Schimmel *et al.* 2011). As shown by Schimmel *et al.* (2011, 2018), PCC is amplitude unbiased and needs no further pre-processing (e.g. time- and frequency-domain normalizations). Another advantage of using PCC and tf-PWS is their higher ability to attenuate incoherent noise, thus facilitating the extraction of EGFs from cross-correlograms. A detailed description of the method can be found in Schimmel *et al.* (2011).

Fig. 3 shows a plot of the resulting EGFs, obtained from the two years of data, displaying interstation distance versus time lag. In the period band investigated (5–30 s), we see that the EGFs are dominated by the Rayleigh-wave fundamental mode. In Fig. 3(a), dispersive Rayleigh wave trains are visible in both causal and acausal branches. We clearly identify the moveout of the wave trains as a function of distance, with an average apparent velocity of ~ 3.0 km s^{-1} . To obtain the final EGFs (Fig. 3b), we phase-weighted stacked the causal and acausal cross-correlograms using tf-PWS.

Finally, we measured the Rayleigh-wave fundamental-mode group velocities on the EGFs following the approach developed by Schimmel *et al.* (2017). This technique uses the S -transform (Stockwell *et al.* 1996) and is equivalent to filtering the EGFs using narrow-band frequency-centred Gaussian filters, as originally proposed by Dziewonski *et al.* (1969). Group-velocity dispersion curves are then obtained by picking the maximum energy in the time–frequency diagrams (see Supporting Information Fig. S1). The frequency higher limit is dictated by energy scattering at high frequencies, whereas the interstation distance controls the lowest analysed frequencies. Empirical practice recommends that interstation distances longer than two/three wavelengths be used to obtain reliable dispersion curves for far-field propagating surface waves. However, Luo *et al.* (2015) showed that cross-correlations with shorter interstation distances, up to only one wavelength, can also be reliable and consistent with those computed for interstation distances longer than three wavelengths. Accordingly, in this study we limited the dispersion curve analysis to the period range between 5.0 and 30.0 s.

Group-velocity uncertainties are estimated using a random sampling and subset tf-PWS approach (Schimmel *et al.* 2017). For each interstation path, several stacks with 50 per cent of all available daily cross-correlations are randomly selected and the group velocity estimated. These subsampled group-velocity dispersion curves are then compared with the reference group-velocity obtained from the stack of the entire data set. This technique provides robust measurements of Rayleigh-wave fundamental-mode group velocities and associated uncertainties. Supporting Information Fig. S1 shows an example of an energy diagram and group-velocity selection. All energy diagrams were visually inspected and inconsistent measurements discarded (see example in Supporting Information Fig. S2). The outliers removed corresponding to ~ 20 per cent of all dispersion curves. The final data set consists of 1034 dispersion curves,

whose distribution by period and interstation distance is shown in Supporting Information Fig. S3. Fig. 4 shows all final group velocities as a function of period, together with the average group velocity. Data uncertainties are in the range 0.01–0.2 km s^{-1} .

3 SURFACE WAVE TOMOGRAPHY

3.1 Methodology

The 3-D tomographic maps were obtained from the dispersion curves in two steps. In the first step, we performed a 2-D inversion to obtain laterally varying group velocities for 22 periods between 7 and 30 s. We discarded dispersion measurements below 7 s due to the low number of interstation paths between 5 and 7 s. In the second step, we inverted the Rayleigh-wave local group velocities to obtain the S -wave velocities as a function of depth.

To quickly evaluate the resolving power of our data set, we conducted a checkerboard test, using the Fast Marching Surface Tomography (FMST) method (Rawlinson & Sambridge 2005). The network geometry provides a dense and azimuthally well-distributed ray path coverage, which results in tomographic images with good resolution (Supporting Information Fig. S4).

We used the 2-D inversion method proposed by Montagner (1986), which is based on the continuous formulation of the inverse problem proposed by Tarantola & Valette (1982), to invert interstation dispersion measurements. Further details on the 2-D inversion method can be found in the Supporting Information. Supporting Information Fig. S5 shows examples of the resulting lateral distribution of group velocities at three chosen periods. In order to quantify the sensitivity of the group velocity of the different periods, we calculated the sensitivity kernels (see Supporting Information Fig. S6). Different wave periods are sensitive to different depths, with the longer periods allowing to sample the structure until a depth of 60 km.

Finally, we inverted the group velocities on a grid of $0.25^\circ \times 0.25^\circ$ in latitude and longitude, to obtain the 3-D V_s model. Because there is a trade-off between crustal velocity and Moho depth, we fixed the Moho depth at each grid point. We used the Moho depths given by Díaz & Gallart (2009) and Dündar *et al.* (2016), smoothed to the lateral resolution of 50 km of our group-velocity maps.

The 3-D inversion scheme that we used follows a novel approach proposed by Haned *et al.* (2016). For a given S -wave velocity model as a function of depth z , $V_s(z)$, synthetic group velocities, $U_{syn}(T_n)$, for periods T_n are computed using the approach of Saito (1988). The S -wave velocity model that explains the observed group velocities $U_{obs}(T_n)$ is determined by minimizing the misfit function between observations ($U_{obs}(T_n)$) and model predictions ($U_{syn}(T_n)$):

$$\chi_d^2 = \frac{1}{N} \sum_{n=1}^N [U_{obs}(T_n) - U_{syn}(T_n)]^2 / \sigma_d^2(T_n), \quad (1)$$

where σ_d is the measurement error.

This inverse problem is non-unique and therefore a condition of smoothness is imposed on $V_s(z)$. On the other hand, the Moho discontinuity must be taken into account. In order to consider both the model smoothness and the Moho discontinuity, $V_s(z)$ is represented as a sum of two terms, as proposed by Haned *et al.* (2016):

$$V_s(z) = V_s^0(z) + \sum_{k=0}^{M-1} V_k N_{k,2}(z), \quad (2)$$

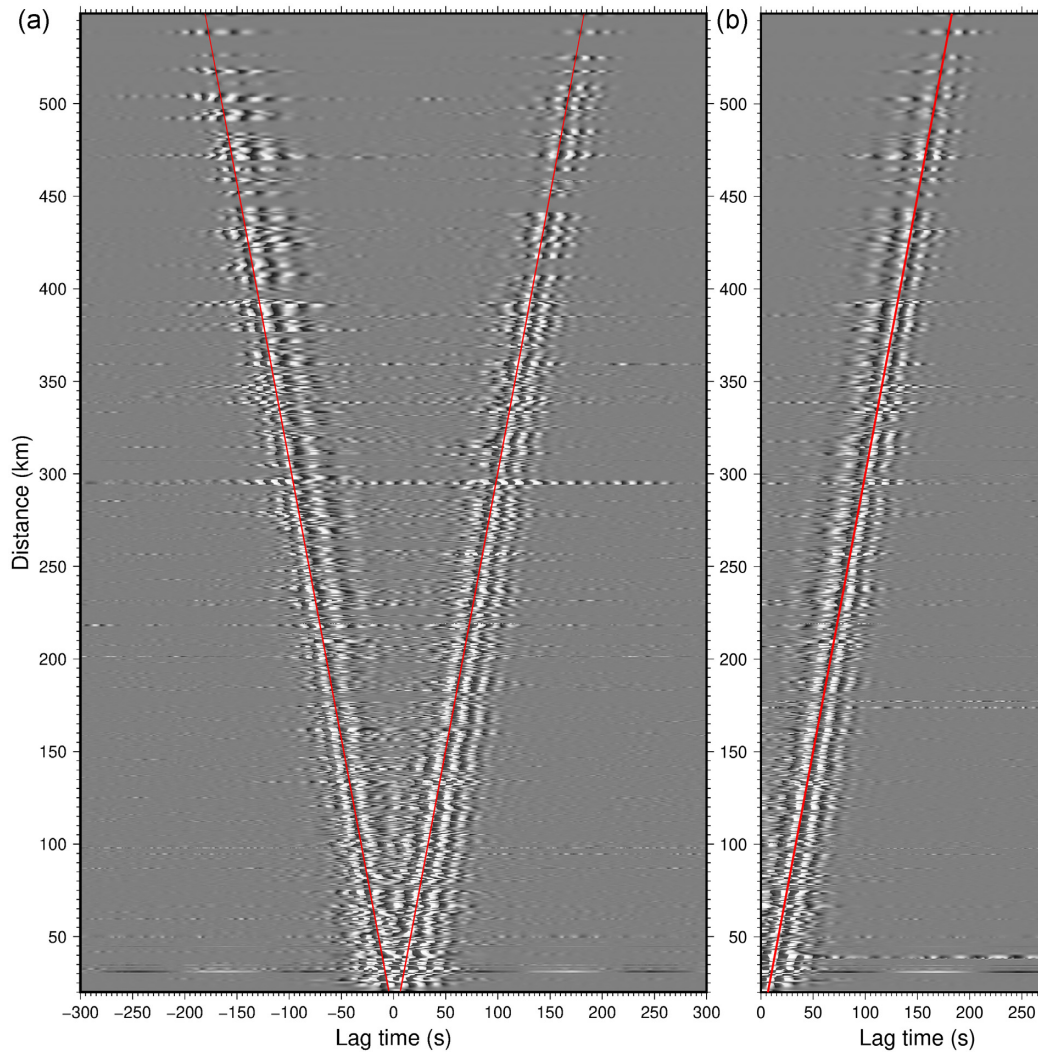


Figure 3. Plot of the EGFs for the entire data set as a function of interstation distance and time. The red lines mark a Rayleigh-wave arrival with a velocity of 3 km s^{-1} . (a) Both causal and acausal lags are displayed. (b) EGFs obtained by phase weighted stack of both causal and acausal phase correlograms.

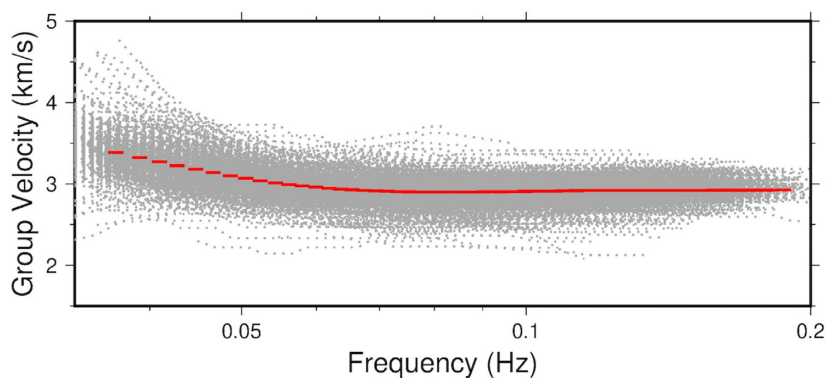


Figure 4. The 1034 group-velocity measurements (grey) corresponding to all selected station pairs as a function of frequency. The average group velocity is plotted in red for comparison.

where $V_S^0(z)$ is the *a priori* model with discontinuities and the second term is a continuous and smooth curve expanded into a series of B-spline basis functions $N_{k,2}(z)$ with weight coefficients V_k . These weight coefficients V_k are the model parameters.

The *a priori* model in the mantle is PREM (Dziewonski & Anderson 1981). For each grid point, the local Moho depth is fixed as explained previously. The local uniform *a priori* velocity $V_S^0(z)$ in the crust can vary. In order to determine it, for a given $V_S^0(z)$, we perform the inversion (described later) and the homogeneity of the

obtained solution $V_S(z)$ is estimated by the following equation:

$$\|V'_S(z)\| = \int [V'_S(z)]^2 dz, \quad (3)$$

where $V'_S(z) = dV_S(z)/dz$ is the depth derivative of the S -wave velocity. This integration is performed over the mantle part of the model down to 80 km depth, excluding the Moho discontinuity. The process is then repeated with different crustal $V_S^0(z)$ in the empirical interval from 2.8 to 4.3 km s⁻¹ until a minimum of $\|V'_S(z)\|$ is achieved. Thus, the crustal *a priori* model is determined by a condition of homogeneity of the inverted model. Note that because the inversion procedure varies $V_S(z)$ by adding splines according to eq. (2), the optimization of the *a priori* velocity $V_S^0(z)$ in the crust means in fact changing only the value of the velocity discontinuity at the Moho depth.

The inversion procedure is a composition of two nested loops (Haned *et al.* 2016): the inner loop computes for a given spline basis $\{N_{k,2}\}$ the optimum model weight coefficients V_k , and the outer loop determines the optimum spline basis which can be defined using a single parameter (M), as described below. The inner loop uses a simulated annealing optimization algorithm (Press 2007, chapter 10.9) to minimize the misfit function (1). The outer loop uses the golden section search in 1-D (Press 2007, chapter 10.1) to minimize *a posteriori* model variance χ_m^2 jointly with the misfit function χ_d^2 . Thus, it provides an optimal level of regularization and enables to determine the single parameter M of the spline basis.

The parameter M is a continuous variable that enables to describe the spline basis. Each spline is defined by four knots along the depth axis and there is an overlap of three knots between two adjacent splines. For a given M we compute d , the distance along the depth axis between the knots of each spline, using equation $d = D/(M + 2)$, where D is the maximum depth of the model (here 85 km). The integer part of M gives the number of splines and the integer of $(M + 3)$ gives the total number of knots. The non-zero fractional part of M gives the compression of the knots toward the surface with the lowest knot being above D .

For any value of M (integer or not), the spline basis thus defined has equidistant knots which are separated by the distance d . But the inversion program uses non-equidistant knots for better performance. The described equidistant knots are converted into the non-equidistant ones through the transformation $y(x) = bx + (1 - b)x^a$, where x is the normalized depth (when $D = 1$), a and b are the parameters in the intervals of $3 < a < 4$, $0.2 < b < 0.4$ as described in Haned *et al.* (2016, see their fig. B1).

When the optimal V_S model has been obtained, the *a posteriori* model variance χ_m^2 is estimated as in Haned *et al.* (2016). To illustrate the effect of the *a priori* crustal model optimization, Fig. 5 shows examples of synthetic data inversion. Synthetic group velocity is calculated for a target model shown by a black line. The panel (a) represents a result of inversion $V_S(z)$ shown by the red line when the crustal optimization is used. We observe almost perfect recovery in the mantle and a smoothed version of two-layered crust since no intercrustal discontinuities are assumed. The optimal *a priori* model $V_S^0(z)$, shown by the blue line, coincides with the target model below the Moho.

In panels (b) and (c), the crustal optimization is not used. The inversion procedure alone requires specifying a crustal *a priori* velocity $V_S^0(z)$. Panels (b) and (c) demonstrate the result of the inversion when the *a priori* $V_S^0(z)$ is underestimated (b) or overestimated (c). In both cases the result of the inversion $V_S(z)$ is distorted, but in a complementary way, that is with $V'_S(z) < 0$ and $V'_S(z) > 0$ in the

mantle right below Moho for (b) and (c), respectively. In all cases shown, the Moho depth is fixed and known independently.

Fig. 6 shows more realistic synthetic tests that consider models with mantle anomalies. The models obtained by inversion are approximated by a small number of layers, which makes them less smooth and more difficult to retrieve. Nonetheless, the inverted V_S models approximate well the target models, both in the case of the low- and high-velocity anomalies in the uppermost mantle.

3.2 Results

Figs 7–9 present the 3-D S -wave model, displayed on selected horizontal planes and vertical profiles. To facilitate the joint interpretation of lithospheric V_S structure, topography and seismicity we also show topographic profiles and the seismicity recorded between 1995 and 2013 (Custódio *et al.* 2015; Veludo *et al.* 2017) on a selected volume around each plane/profile.

Fig. 7 shows the V_S model at different depths, ranging from 5 to 60 km, together with a topographic map and the main tectonic features from Fig. 1(a) superimposed. In particular, the limits of the main tectonic units are plotted as grey dashed lines. Velocity perturbations are presented in percentage with respect to the average V_S at each depth. The laterally variable V_S increase at the Moho may therefore introduce contrasts in the velocities at a given depth. As such, at 25 and 30 km depths, we computed the V_S perturbations by taking into account whether each cell was still in the crust or already in the mantle, according to the predicted Moho depth. The crustal thickness ranges between 24 and 34 km, with an average of 30 km; therefore, the first four subplots (b–e) reflect the crustal structure whereas the last two (40 and 60 km depth) (h and i) show the uppermost mantle.

At most depths, the velocity anomalies are relatively smooth, as would be expected from a surface wave tomography, and vary in the interval between -10 and $+10$ per cent. At 5 km, most anomalies follow the limits of the Variscan contacts associated with the Ibero-Armorican Arc and their interception with the more recent alpine structures (LB and AB basins). In the crust, most positive anomalies are located in the Variscan domain, with some extending down to 60 km, namely in the north of Portugal. The Alpine inverted basins correspond to negative anomalies with a shallower expression.

Figs 8 and 9 present several vertical profiles that extend from 5 to 60 km depth, together with the corresponding topographic profile (with vertical exaggeration). For reference, the Moho depths from Díaz *et al.* (2015) and Dündar *et al.* (2016) are plotted on the vertical profiles as grey dashed lines.

In the Supporting Information, we further show the characteristic dispersion curves for the different tectonic units (Fig. S7). The curves exhibit a clear regional variation, with those of the sedimentary basins and of the South Portuguese Zone (SPZ) presenting lower group velocities at short periods.

4 DISCUSSION

The comparison between surface features (Fig. 1) and V_S at depth (Fig. 7) shows that the surface features seem to extend into the upper crust, roughly down to 15 km depth. However, this good association changes significantly for the lower crust and uppermost mantle. In the upper-middle crust, down to ~ 20 km depth, the V_S model is consistent with the results of the local earthquake tomography of Veludo *et al.* (2017).

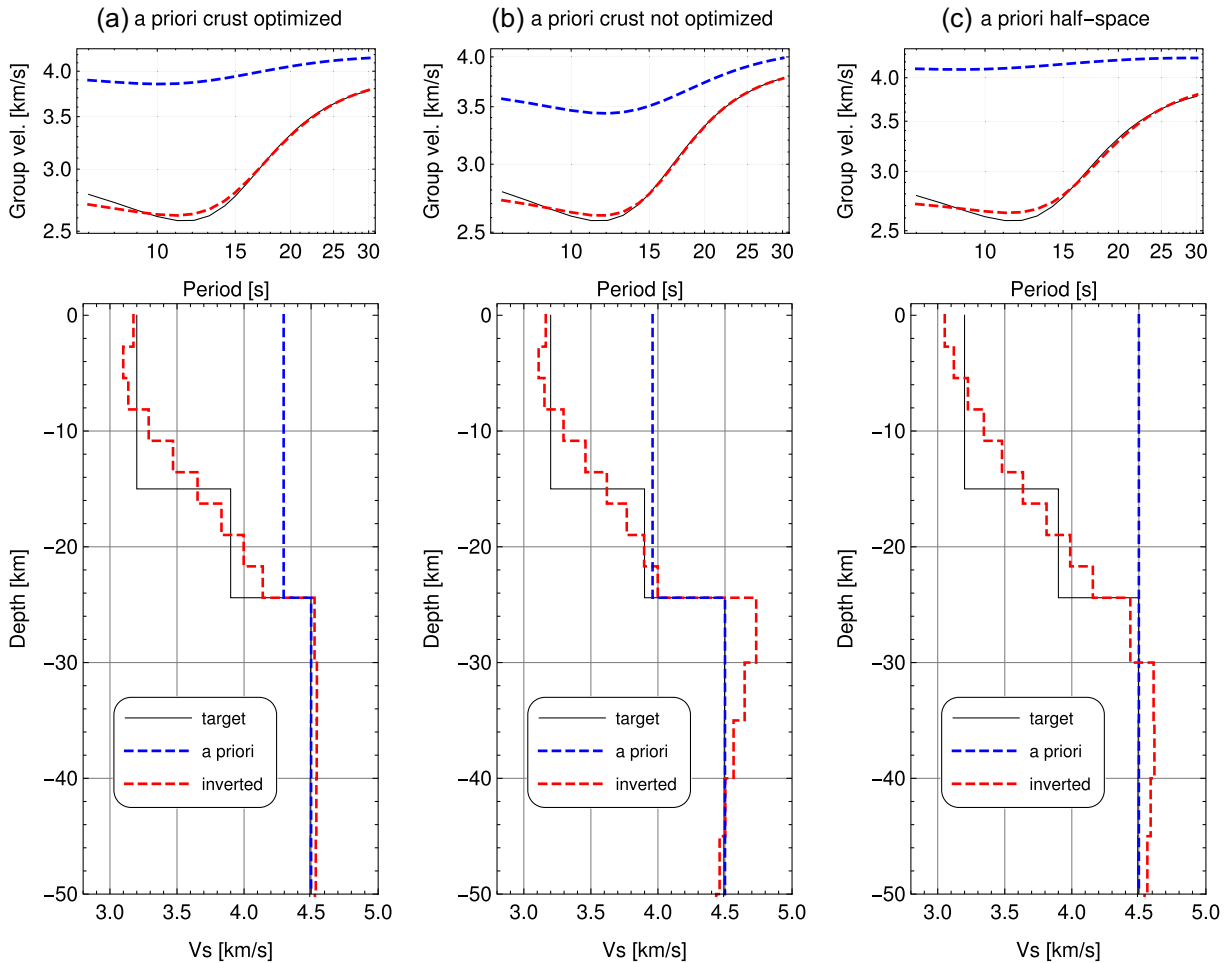


Figure 5. Synthetic inversions of group velocities. The target model and the result of inversion are shown by black and red lines, respectively. The blue line shows the *a priori* model used. (a) Using an *a priori* crustal model that was optimized. (b) Using a non-optimized underestimated *a priori* velocity $V_S^0(z)$. The result is distorted in the uppermost mantle and $V_S'(z) < 0$. (c) Using a non-optimized overestimated *a priori* velocity $V_S^0(z)$. The result is also distorted but with $V_S'(z) > 0$ in the uppermost mantle (24–40 km).

4.1 Galícia Trás-os-Montes Zone

To the North, in the area corresponding to the Galícia Trás-os-Montes Zone (around 41.5°N, **GTMZ** in Fig. 7a), we image a shallow strong positive anomaly that extends down to 15 km depth. This positive anomaly is roughly limited by the Penacova-Régua-Verín Fault system (PRV in Fig. 1b). The southeast of the GTMZ sector presents a negative anomaly down to 10 km, followed by a positive anomaly below and then another negative anomaly in the lower crust. This positive anomaly with a thin overlying low-velocity layer, also shown in profile E-E' in Fig. 9, is consistent with the pile of allochthonous thrust sheets that compose the peculiar tectonic unit called Morais and Bragança massifs, overlying the autochthonous Central Iberian Zone (CIZ; Dias & Ribeiro 1995; Simancas *et al.* 2001; Ribeiro *et al.* 2007; Arenas *et al.* 2016b). Further, profiles E-E' and G-G' (Fig. 9) are also consistent also with a crustal thickening to the NE sector of Portugal, as previously suggested by receiver function results (Dündar *et al.* 2016).

In sum, most positive velocities anomalies in the GTMZ seem to be confined to the upper crust, consistent with previous results (e.g. Attanayake *et al.* 2017 or Veludo *et al.* 2017), and in agreement with the presence of a thin shell, composed of allochthonous thrust sheets overlying the CIZ. As an exception to this result, we image

only a low-velocity anomaly roughly centered around the PRV fault system.

4.2 Central Iberian Zone

The Central Iberian Zone (**CIZ**) presents a weak gradient between areas of low and high velocities, pointing to a relatively homogenous velocity structure. Its western sector has higher V_S values than the eastern sector, and the limit between the two roughly coincides with the Manteigas-Vilarica-Bragança fault system (MVB in Fig. 1b). This observation is consistent with the V_p values of Veludo *et al.* (2017) for the upper and middle crust. Newly imaged in our tomography is the extension of that velocity contrast into the upper mantle, suggesting that the NNE–SSW MVB fault system is a lithospheric-scale feature. It should be noted that the MVB fault is marked by instrumental seismicity at crustal level. On the other hand, the NE–SW Seia-Lousã and Ponsul faults (SL and Po in Fig. 1) correspond to only minor structural contrasts in our model.

The vertical profiles of Figs 8 and 9 also show that the upper mantle structure beneath the CIZ is relatively homogenous, as expected from the Variscan core unit, with exception of the lower crust anomaly located in the CIZ-OMZ, south of the Po fault and discussed below.

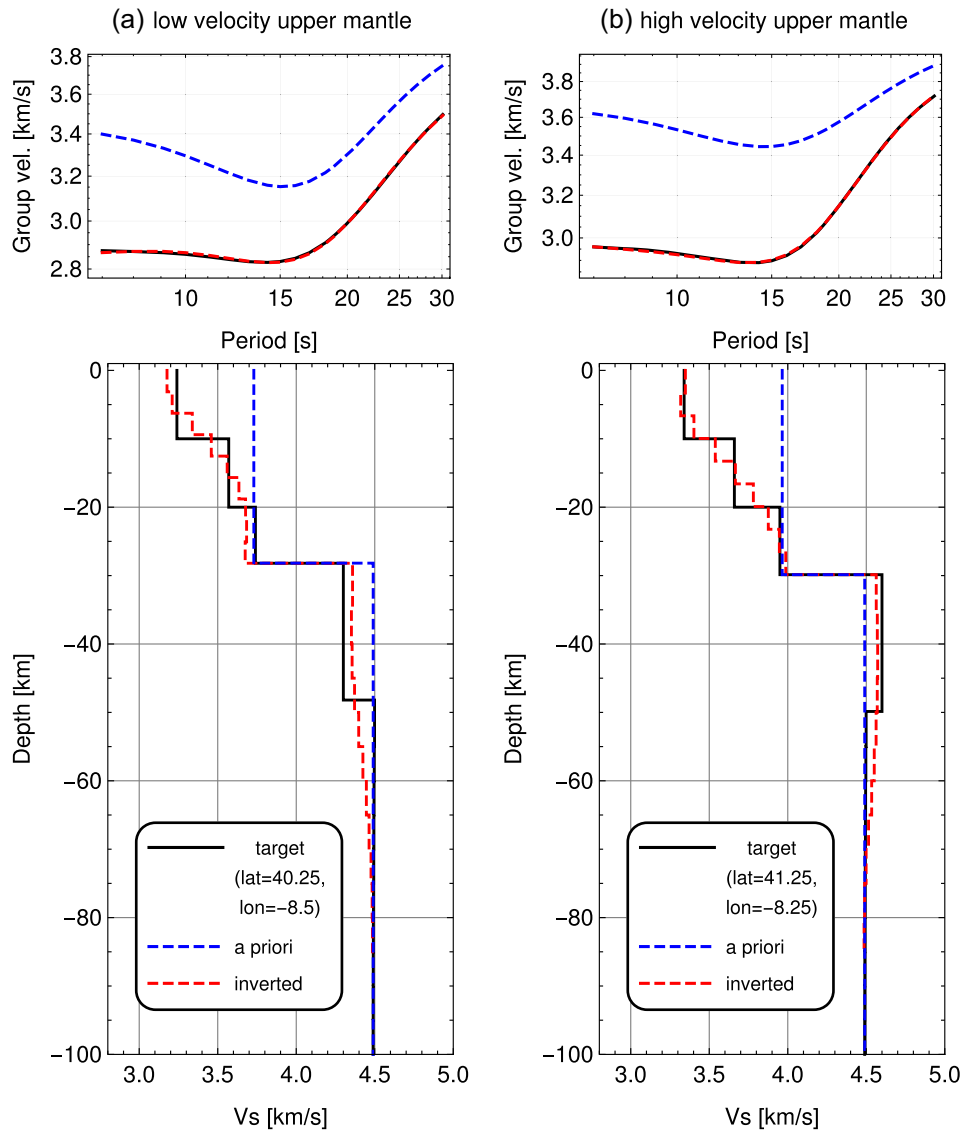


Figure 6. (a) Synthetic tests with a mantle anomaly. The target model (black) with a low-velocity uppermost mantle is taken at latitude 40.25° and longitude -8.5° . The number of layers is reduced to 3 in crust and 2 in mantle. The result of inversion is shown in red. (b) The same as (a), but for a model at latitude 41.25° and longitude -8.25° with a high-velocity uppermost mantle.

The contrast between the CIZ (fast V_s) and the adjacent tectonic units (low V_s)—OMZ to the south and LB to the west—is very clear at a shallow level (5 km, Fig. 7b). The OMZ-CIZ is roughly coincident with the Tomar-Badajoz-Córdoba shear zone (TBC in Fig. 1b). At depths of 10–20 km, the pattern across the OMZ-CIZ is inverted, highlighting a contact between a relatively slow CIZ to the north and a relatively fast OMZ to the south (Fig. 7e).

4.3 Ossa Morena Zone

The Ossa Morena Zone (OMZ) is one of the most distinguished tectonic features in our tomographic model, marked by a strong fast V_s anomaly over most of the crust (5–25 km, Figs 7b–f). However, Fig. 7 also shows that the OMZ is segmented into two sectors, the limit of which is roughly parallel to the CIZ-OMZ contact, along the Ciborro-Serra da Ossa alignments, and marked by a relatively intense seismic alignment, previously noted by Veludo *et al.* (2017) and Matos *et al.* (2018), who called it the Arraiolos Seismic Zone

(Arl in Fig. 1b). At upper-middle crustal levels (5–25 km depth), V_s changes from slow to the north of this alignment to fast to its south, consistent with results from local earthquake tomography (Veludo *et al.* 2017) and magnetotelluric 2-D profiles (Almeida *et al.* 2005).

Deeper, in the middle-lower crust and extending into the upper mantle (25–60 km depth, Figs 7f–i), our tomographic model shows a previously unknown low-velocity anomaly, located at $\sim 39.3^\circ\text{N}$, roughly where the CIZ-OMZ-LTSB contacts intersect. This strong low-velocity anomaly, seems to start at the base of the crust and to increasing in amplitude into the uppermost mantle, where it becomes a dominant signal. The vertical profiles C-C' (Fig. 8) and H-G' (Fig. 9) display the lateral variation across this well-marked transition (~ 38.8 – 39°N), extending into the mantle, where the velocity contrast increases.

The analysis of profiles B-B', C-C' and D-D' in Fig. 8 and H-G' in Fig. 9 suggests the presence of a low-velocity body, maybe of lenticular shape, located at the base of the crust roughly at the contact

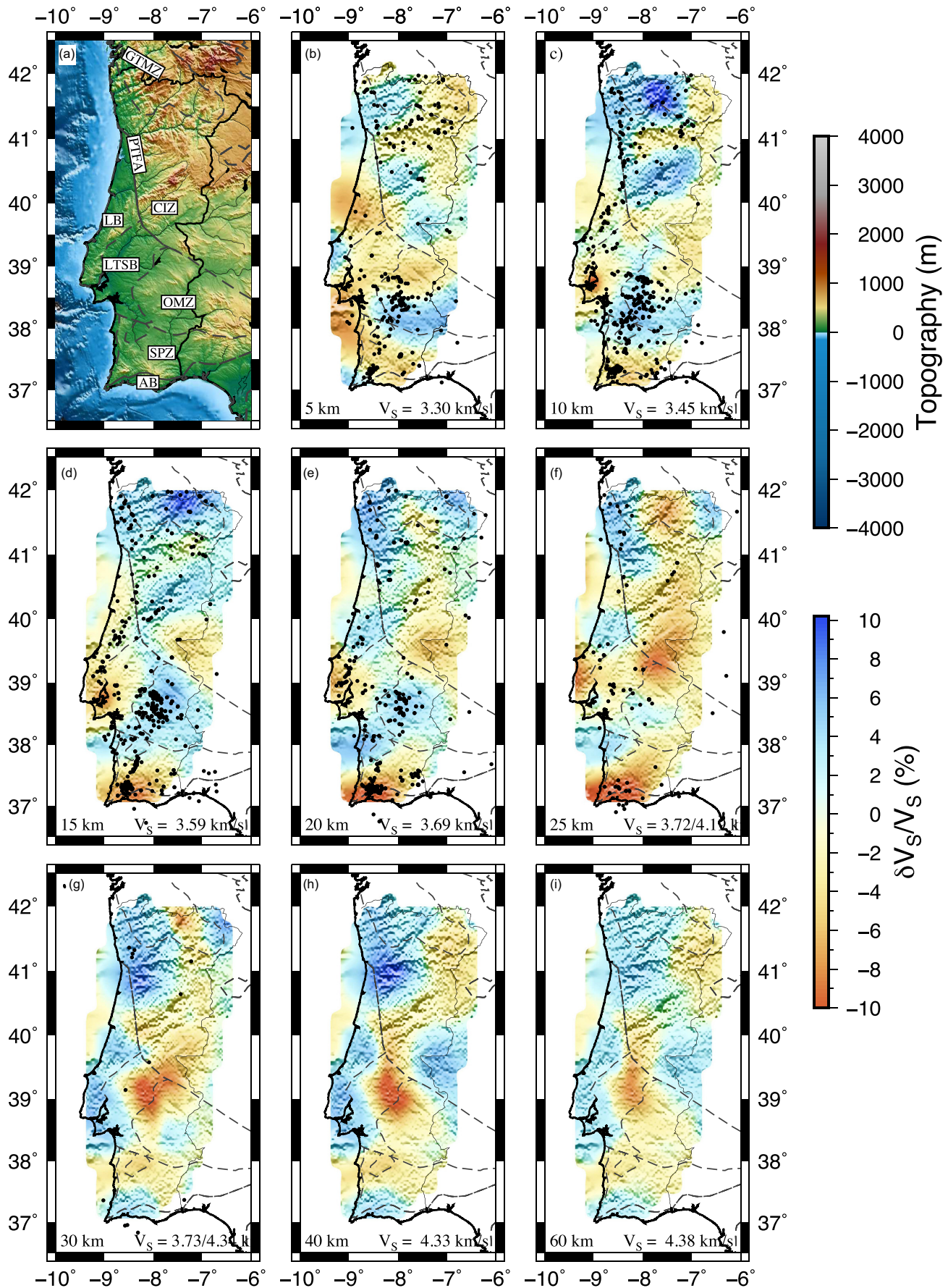


Figure 7. (a) Topographic map, limits of the main tectonic units (grey dashed lines) and seismicity recorded between 2000 and 2014 relocated by Veludo *et al.* (2017), black dots. (b–i) S -wave velocity maps at different depths. Velocity perturbations are displayed in percentage with respect to the average model. Depth and the V_S average are indicated at the bottom of each map. At 25 and 30 km, the average was computed separately for cells above and beneath the Moho (Díaz & Gallart 2009; Dündar *et al.* 2016). Earthquakes are plotted in a volume of ± 2 km around each depth.

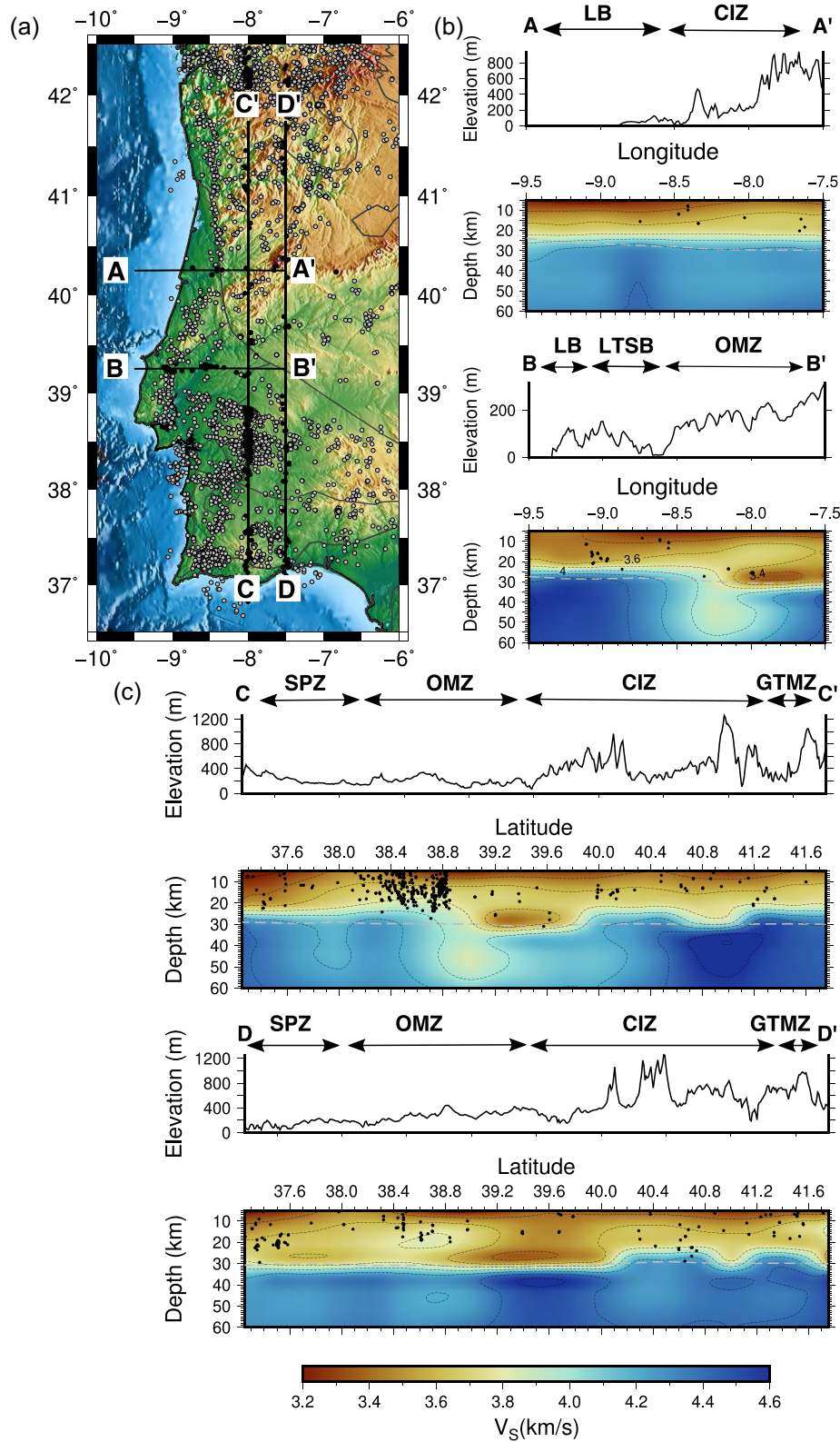


Figure 8. Vertical profiles through the 3-D S -wave velocity model. (a) Topographic map with the position of four vertical profiles. Earthquakes recorded between 1995 and 2013 are plotted as grey dots or as black dots if they are close to the selected profiles. (b) Two W–E profiles crossing the LB and (c) two N–S profiles crossing the Arroios seismic zone. All profiles are coincident with vertical node planes. S -wave velocities are plotted as absolute values. Earthquakes, relocated by Veludo *et al.* (2017), are plotted around the latitude (b) and longitude (c) of the profiles within an interval of $\pm 0.05^\circ$.

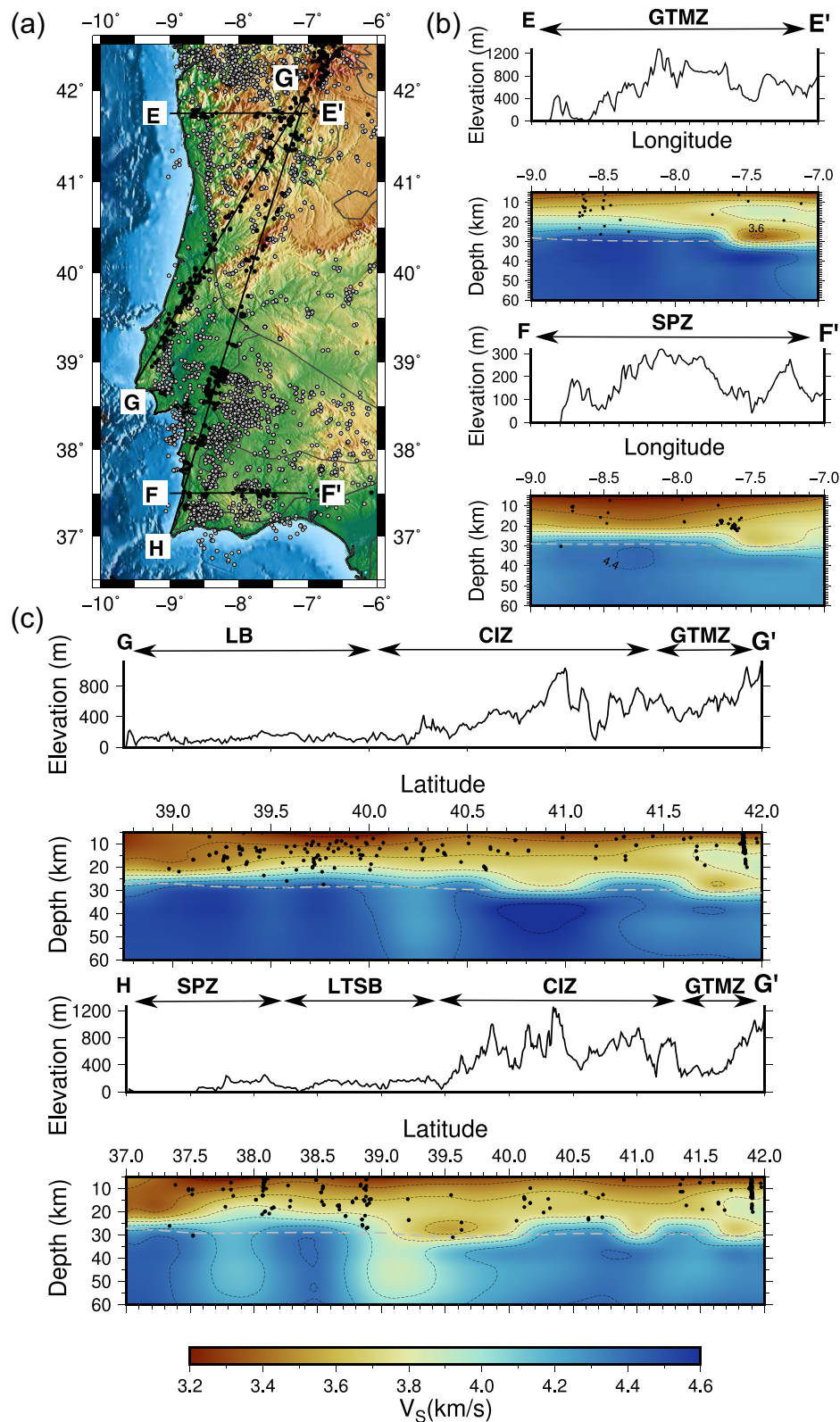


Figure 9. Vertical profiles through the 3-D S-wave velocity model. (a) Topographic map with the position of the four vertical profiles. Earthquakes recorded between 1995 and 2013 are plotted in grey or black dots if they are close to the selected profiles. (b) Profiles crossing the GMTZ (E–E′) and the SPZ (F–F′) zones. (c) Profiles along the contact between the LB and LTSB basins (G–G′) and crossing all of Portugal from southwest to northeast (H–G′). S-wave velocities are plotted as absolute values. Earthquakes, relocated by Veludo *et al.* (2017), are plotted around the plotted profiles within an interval of $\pm 0.05^\circ$.

between the CIZ and the OMZ, and limited to the south by something akin to a low-velocity wedge that extends into the mantle. This negative velocity anomaly may correspond to an anomaly identified in *S*-wave models obtained from teleseismic tomography, located roughly beneath the OMZ (Monna *et al.* 2013; Civiero *et al.* 2019) and which extends down to 190 km depth. Attanayake *et al.* (2017) also obtained low velocities in this region at 25 km depth, the deepest level in their study. The model proposed by Palomeras *et al.* (2017) for the entire Iberian Peninsula does not exhibit a clear low-velocity anomaly in this region. However, their data set had a much sparser coverage in Portugal compared to the rest of the peninsula. Simancas *et al.* (2013) already reported the presence of anomalous bodies in the deep crust in this region, albeit associated with high V_p velocities, which they associated with structurally layered mafic/ultramafic bodies that intruded along a midcrustal decollement.

The nature of the OMZ as a Variscan accretionary wedge between the CIZ and the SPZ may explain the observed V_s structure, with lower velocities to its north associated with subducted material with stronger sedimentary content, and a southern part composed of harder, more brittle and faster material, also explaining the concentration of ongoing seismic activity. The strong low-velocity anomaly in the lower crust beneath the OMZ-CIZ limit suggests a complex structure associated with the past tectonic processes. For depths larger than 10 km and down to 30 km, the OMZ high velocity anomaly seems to extend further to the west coast, while receding from the east.

We note that the regions with low V_s anomalies in the southern CIZ and northern OMZ are devoid of earthquakes. This suggests that seismic deformation concentrates in the regions of faster seismic velocities, eventually corresponding to more brittle rocks.

4.4 South Portuguese Zone

The South Portuguese Zone (SPZ) is mostly characterized by a persistent low-velocity anomaly that extends into the mantle. The OMZ-SPZ contact is very sharp from 5 km down to 20 km depth, remaining visible around 30 km depth, and shows fast velocities to the north (OMZ) and slow velocities to the south (SPZ; Fig. 7). However, at upper levels (5–10 km), this velocity contrast seems to match better the Albornoa-Aljustrel-Messejana Alignment (AAM in Fig. 1b), that is the southern limit of the Iberian Pyrite Belt, than the OMZ-SPZ contact itself, corresponding to the Beja ophiolitic complex. These results are consistent with those obtained in the V_p model of Veludo *et al.* (2017). Inside the SPZ there is a hint of a W–E increase in V_s velocities also present in their V_p model. The Southwestern tip of the Algarve, roughly starting at the Monchique Massif (M in Fig. 1b) appears as a distinct feature from the rest of the SPZ, either marked by strong low velocities at shallow levels or by high velocity anomalies at depth. This sector has been recognized as a piece of anomalous crust in several studies (see Dias & Ribeiro 1995; Simancas *et al.* 2001; Ribeiro *et al.* 2007; Arenas *et al.* 2016b; Veludo *et al.* 2017). Being at the edge of our model, we cannot discriminate its exact nature.

4.5 The Mesozoic basins

In the Mesozoic basins (Fig. 1a), at shallow depths, the **LB**, the **LTSB** and the **AB** all display low *S*-wave velocities, as expected, corresponding to sedimentary rocks.

The **LB** is clearly marked in the upper crust by a low-velocity anomaly in the upper 5 km (Fig. 7b). Its eastern border is marked by a low-high velocity contact that coincides with the Porto-Tomar-Ferreira do Alentejo shear zone (PTFA in Fig. 1b). Unlike in previous results (e.g. Veludo *et al.* 2017), it is not possible to access the dip of the PTFA fault or the exact depth extension of the basin. However, the imaged higher velocities in the mantle (profile A-A', ~8.7°W, Fig. 8) suggest a lithospheric-scale nature of this contact. This contact, well imaged near the surface and at deeper mantle levels, fades at mid-crustal levels, eventually due to the inclination of the contact and/or to the increase in velocities of the Estremadura Limestone Massif, limited by the Nazaré-Condeixa-Alvaiázere fault system (NCA in Fig. 1b).

The **LTSB** corresponds to a strong low V_s anomaly, which appears to vanish at mid-crustal levels ~15–20 km in Fig. 7.

The **AB** is located on the southernmost part of the model, with few rays crossing it, therefore poorly imaged in our model. However, its low-velocity anomaly is visible in the entire crust, until 25 km depth. Still, it could be a smearing effect from the structure beneath Monchique.

5 CONCLUSIONS

Phase cross-correlation and phase weighted stack of 24 months of continuous seismic data, recorded at 64 stations, enabled us to retrieve high-quality EGFs. We were thus able to infer a high-resolution *S*-wave tomographic model of Portugal, particularly in the area of the WILAS project. We adapted the trans-dimensional inversion method presented in Haned *et al.* (2016) to optimize the *a priori* crustal model within the inversion scheme to obtain the shear wave velocity. The 3-D inversion enabled to obtain the crustal and uppermost mantle structure across Portugal.

We found a good correlation with surface geology, in particular at upper and middle crust levels. The different tectonic units of the Variscan Massif and Mesozoic basins, as well as their contacts, in general match the observed V_s anomaly pattern. Some important fault systems, like the MVB or the PTFA, have expression down to the mantle whereas others seem to be limited to the upper crust. In general, our results support a smoothly varying crust–mantle transition, as observed in Dündar *et al.* (2016), in particular beneath the CIZ and SPZ. In the NE Portugal, the V_s model revealed the presence of a middle crust high velocity anomaly associated with a pile of allochthonous thrust sheets that compose the peculiar tectonic unit of the Morais and Bragança massifs overlying the autochthonous Central Iberian Zone (CIZ).

In the OMZ, the accretionary wedge nature associated with the Variscan suture is clear at upper crustal levels and is characterized by a strong lateral velocity variation across the CIZ-OMZ contact and with a low V_s anomaly extending into the uppermost mantle.

The strongest signal in our 3-D tomographic model is a previously unknown low-velocity anomaly, roughly cylindrical in shape and located below the CIZ-OMZ transition. This anomaly is very strong in the upper mantle and lower crust but fades into the middle crust. This anomaly may be due to low-velocity material, probably of sedimentary origin, subducted along the OMZ-CIZ contact, concentrating in the lower crust. This low-velocity anomaly coincides with a region of seismic quiescence and may act as an aseismic wedge between two different deformation sectors, one to the south and the other to the north.

Our shear wave velocity model for the crust and uppermost mantle contributes to constraining the main tectonic units at depth, filling

the gap between the crustal-scale local earthquake tomography and the mantle scale body-wave tomographic models. In the future, we intend to include both crustal azimuthal and radial anisotropy in our 3-D model, which will provide a better insight into the crustal stress in the various tectonic units. Future deployments of regularly spaced seismic stations will allow to invert for azimuthal anisotropy. Cross-correlation of the horizontal components will also allow to compute Love waves, which jointly with Rayleigh waves can provide the radial anisotropy.

ACKNOWLEDGMENTS

We acknowledge all institutions providing seismic data used in this research: FCT project WILAS-West Iberia Lithosphere and Asthenosphere Structure (doi:10.14470/3n7565750319), Instituto Português do Mar e da Atmosfera (IPMA) Seismic Network, University of Lisbon Seismic Network and Deep Ocean Test Array (DOCTAR) project (Hannemann *et al.* 2014, 2016, 2017). WILAS temporary stations and DOCTAR stations were provided by the Geophysical Instrument Pool Potsdam (GIPP). MS thanks the Ministerio de Ciencia, Innovación y Universidades (project SANIMS, RTI2018-095594-B-I00) and Generalitat de Catalunya (2017SGR1022). This publication is a contribution to different FCT projects SIGHT (PTDC/CTA-GEF/30264/2017), RESTLESS (PTDC/CTA-GEF/6674/2020), WILAS (PTDC/CTE-GIX/097946/2008), SQUAREL (PTDC/CTE-GIX/116819/2010) and SPIDER (PTDC/GEO-FIQ/2590/2014). This work is also developed in the framework of FCT UIDB/50029/2020—Instituto Dom Luiz. Most figures were plotted using the GMT—Generic Mapping Tools software (Wessel *et al.* 2013). Data pre-processing was done using SAC—Seismic Analysis code (Goldstein & Snoke 2005).

DATA AVAILABILITY

Data from WILAS temporary network (code 8A) are available in GEOFON at doi:10.14470/3N7565750319. Data from IPMA permanent stations are available in IPMA at <http://ceida.ipma.pt>. Data from the DOCTAR array (code Y7) are in GEOFON (URL: <https://geofon.gfz-potsdam.de/waveform/archive/network.php?ncode=Y7&year=2011>) under restricted access.

REFERENCES

- Afilhado, A., Matias, L., Shiobara, H., Hirn, A., Mendes-Victor, L. & Shimamura, H., 2008. From unthinned continent to ocean: the deep structure of the West Iberia passive continental margin at 38°N, *Tectonophysics*, **458**(1–4), 9–50.
- Almeida, E., Monteiro Santos, F., Mateus, A., Heise, W. & Pous, J., 2005. Magnetotelluric measurements in SW Iberia: new data for the Variscan crustal structures, *Geophys. Res. Lett.*, **32**, 1–4.
- Arenas, R. *et al.*, 2016a. The Galicia–Ossa-Morena Zone: proposal for a new zone of the Iberian Massif. Variscan implications, *Tectonophysics*, **681**, 135–143.
- Arenas, R. *et al.*, 2016b. Allochthonous terranes involved in the Variscan suture of NW Iberia: a review of their origin and tectonothermal evolution, *Earth-Sci. Rev.*, **161**, 140–178.
- Attanayake, J., Ferreira, A. M., Berbellini, A. & Morelli, A., 2017. Crustal structure beneath Portugal from teleseismic Rayleigh wave ellipticity, *Tectonophysics*, **712**, 344–361.
- Bensen, G.D., Ritzwoller, M.H., Barmin, M.P., Levshin, A.L., Lin, F.-C., Moschetti, M.P., Shapiro, N.M. & Yang, Y., 2007. Processing seismic ambient noise data to obtain reliable broad-band surface wave dispersion measurements, *Geophys. J. Int.*, **169**, 1239–1260.
- Bensen, G.D., Ritzwoller, M.H. & Shapiro, N.M., 2008. Broadband ambient noise surface wave tomography across the United States, *J. geophys. Res.*, **113**(B5). doi:10.1029/2007JB005248.
- Carbonell, R. *et al.*, 2004. Geophysical evidence of a mantle derived intrusion in SW Iberia, *Geophys. Res. Lett.*, **31**, L11601, doi:10.1029/2004GL019684.
- Carrilho, F. *et al.*, 2021. The Portuguese National Seismic Network—products and services, *Seismol. Res. Lett.*, **92**, 1541–1570.
- Civiero, C., Custódio, S., Rawlinson, N., Strak, V., Silveira, G., Arroucau, P. & Corela, C., 2019. Thermal nature of mantle upwellings below the Ibero-western Maghreb region inferred from teleseismic tomography, *J. geophys. Res.*, **124**(2), 1781–1801.
- Civiero, C., Strak, V., Custódio, S., Silveira, G., Rawlinson, N., Arroucau, P. & Corela, C., 2018. A common deep source for upper-mantle upwellings below the Ibero-western Maghreb region from teleseismic P-wave travel-time tomography, *Earth planet. Sci. Lett.*, **499**, 157–172.
- Corela, C., Silveira, G., Matias, L., Schimmel, M. & Geisler, W., 2017. Ambient seismic noise tomography of SW Iberia integrating seafloor- and land-based data, *Tectonophysics*, **700**, 131–149.
- Custódio, S., Dias, N. A., Carrilho, F., Góngora, E., Rio, I., Marreiros, C., Morais, I., Alves, P. & Matias, L., 2015. Earthquakes in western Iberia: improving the understanding of lithospheric deformation in a slowly deforming region, *Geophys. J. Int.*, **203**, 127–145.
- Custódio, S., Dias, N.A., Caldeira, B., Carrilho, F., Carvalho, S., Corela, C., Diaz, J., Narciso, J., Madureira, G., Matias, L., Haberland, C. & team, WILAS, 2014. Ambient noise recorded by a dense broadband seismic deployment in western Iberia, *Bull. seism. Soc. Am.*, **104**(6), 2985–3007.
- De Vicente, G., Cloetingh, S., Van Wees, J.D. & Cunha, P.P., 2011. Tectonic classification of Cenozoic Iberian foreland basins, *Tectonophysics*, **502**(1–2), 38–61.
- Dias, N.A., Silveira, G. & Haberland, C., 2010. Data of the temporary seismic WILAS network. GFZ Data Services. Other/Seismic Network. doi:10.14470/3N7565750319.
- Dias, R. & Ribeiro, A., 1995. The Ibero-Armorican Arc: a collision effect against an irregular continent?, *Tectonophysics*, **246**, 113–128.
- Diaz, J. & Gallart, J., 2009. Crustal structure beneath the Iberian Peninsula and surrounding waters: a new compilation of deep seismic sounding results, *Phys. Earth planet. Inter.*, **173**, 181–190.
- Diaz, J., Gallart, J., Morais, I., Silveira, G., Pulgar, J.A., Dias, N. A., Ruiz, M. & González-Cortina, J.-M., 2015. From the Bay of Biscay to the High Atlas: completing the anisotropic characterization of the westernmost Mediterranean region, *Tectonophysics*, **663**, 192–202.
- Dündar, S., Dias, N.A., Silveira, G., Kind, R., Vinnik, L., Matias, L. & Bianchi, M., 2016. Estimation of the crustal bulk properties beneath mainland Portugal from P receiver functions, *Pure appl. Geophys.*, **173**, 1949–1970.
- Dziewonski, A. M. & Anderson, D. L., 1981. Preliminary reference earth model, *Phys. Earth planet. Inter.*, **25**(4), 297–356.
- Dziewonski, A., Bloch, S. & Landisman, M., 1969. A technique for the analysis of transient seismic signals, *Bull. seism. Soc. Am.*, **59**, 427–444.
- Fernandes, R. M. S., Ambrosius, B. A. C., Noomen, R., Bastos, L., Wortel, M. J. R., Spakman, W. & Govers, R., 2003. The relative motion between Africa and Eurasia as derived from ITRF2000 and GPS data, *Geophys. Res. Lett.*, **30**(16), doi:10.1029/2003GL017089.
- Flecha, I., Palomeras, I., Carbonell, R., Simancas, F., Ayarza, P., Matas, J., González-Lodeiro, F. & Pérez-Estaún, A., 2009. Seismic imaging and modelling of the lithosphere of SW-Iberia, *Tectonophysics*, **472**, 148–157.
- GEOFON Data Centre, 1993. GEOFON Seismic Network, Deutsches Geoforschungszentrum GFZ. doi:10.14470/TR560404.
- Goldstein, P. & Snoke, A., 2005. “SAC Availability for the IRIS Community”, Incorporated Institutions for Seismology Data Management Center Electronic Newsletter.7(UCRL-JRNL-211140)
- Haned, A., Stutzmann, E., Schimmel, M., Kiselev, S., Davaille, A. & Yelles-Chouaie, A., 2016. Global tomography using seismic hum, *Geophys. J. Int.*, **204**(2), 1222–1236.
- Hannemann, K., Krüger, F., Dahm, T. & Lange, D., 2016. Oceanic lithospheric S-wave velocities from the analysis of P-wave polarization at the

- ocean floor, *Geophysical Supplements to the Monthly Notices of the Royal Astronomical Society*, **207**(), 1796–1817.
- Hannemann, K., Krüger, F., Dahm, T. & Lange, D., 2017. Structure of the oceanic lithosphere and upper mantle north of the Gloria fault in the eastern mid-Atlantic by receiver function analysis, *Journal of Geophysical Research: Solid Earth*, **122**(), 7927–7950.
- Hannemann, K., Krüger, F. & Dahm, T., 2014. Measuring of clock drift rates and static time offsets of ocean bottom stations by means of ambient noise, *Geophysical Journal International*, **196**(), 1034–1042.
- Instituto Dom Luiz (IDL)-Faculdade De Ciências Da Universidade De Lisboa, 2003. University of Lisbon Seismic Network, International Federation of Digital Seismograph Networks, doi:10.7914/SN/LX.
- Instituto Português do Mar e da Atmosfera, I.P., 2006. Portuguese National Seismic Network, International Federation of Digital Seismograph Networks, doi:10.7914/SN/PM.
- Jeannot, L., Kuszniir, N., Mohn, G., Manatschal, G. & Cowie, L., 2016. Constraining lithosphere deformation modes during continental breakup for the Iberia–Newfoundland conjugate rifted margins, *Tectonophysics*, **680**, 28–49.
- Linnemann, U., Pereira, M.F., Jeffries, T.E., Drost, K. & Gerdes, A., 2008. The Cadomian Orogeny and the opening of the Rheic Ocean: the diacrony of geotectonic processes constrained by LA-ICP-MS U–Pb zircon dating (Ossa-Morena and Saxo-Thuringian Zones, Iberian and Bohemian Massifs), *Tectonophysics*, **461**, 21–43.
- Luo, Y., Yang, Y., Xu, Y., Xu, H., Zhao, K. & Wang, K., 2015. On the limitations of interstation distances in ambient noise tomography, *Geophys. J. Int.*, **201**(2), 652–661.
- Matias, L., 1996. A sismologia experimental na modelação da crosta em Portugal Continental, *PhD thesis*, University of Lisbon, Lisbon.
- Matos, C., Custodio, S., Batlo, J., Zahradnik, J., Arroucau, P., Silveira, G. & Heimann, S., 2018. An active seismic zone in intraplate west Iberia inferred from high-resolution geophysical data, *J. geophys. Res.*, **123**(4), 2885–2907.
- Matte, P., 1986. Tectonics and plate tectonics model for the Variscan belt of Europe, *Tectonophysics*, **126**, 329–374.
- Matte, P., 1991. Accretionary history and crustal evolution of the Variscan belt in Western Europe, *Tectonophysics*, **196**, 309–337.
- Matte, P., 2001. The Variscan collage and orogeny (480–290 Ma) and the tectonic definition of the Armorica microplate: a review, *Terra Nova*, **13**, 122–128.
- Monna, S., Cimini, G. B., Montuori, C., Matias, L., Geissler, W. & Favali, P., 2013. New insights from seismic tomography on the complex geodynamic evolution of two adjacent domains: Gulf of Cadiz and Alboran Sea, *Journal of Geophysical Research: Solid Earth*, **118**(4), 1587–1601.
- Montagner, J.-P., 1986. Regional three-dimensional structures using long-period surface waves, *Ann. Geophys. Terr. Planet. Phys.*, **4**, 283–294.
- Palomeras, I. et al., 2009. Nature of the lithosphere across the Variscan orogen of SW Iberia: dense wide-angle seismic reflection data, *J. geophys. Res.*, **114**, 1–29.
- Palomeras, I., Villaseñor, A., Thurner, S., Levander, A., Gallart, J. & Harnafi, M., 2017. Lithospheric structure of Iberia and Morocco using finite-frequency Rayleigh wave tomography from earthquakes and seismic ambient noise, *Geochim. Geophys. Geosyst.*, **18**(5), 1824–1840.
- Pereira, R. & Alves, T.M., 2013. Crustal deformation and submarine canyon incision in a Meso-Cenozoic first-order transfer zone (SW Iberia, North Atlantic Ocean), *Tectonophysics*, **601**, 148–162.
- Pereira, R., Alves, T.M. & Mata, J., 2016. Alternating crustal architecture in West Iberia: a review of its significance in the context of NE Atlantic rifting, *J. geol. Soc. Lond.*, doi:10.1144/jgs2016-050.
- Pinheiro, L., Wilson, R., Pena dos Reis, R., Whitmarsh, R. & Ribeiro, A., 1996. The western Iberia margin: a geophysical and geological overview, in *Proceedings-ocean Drilling Program Scientific Results*, pp. 3–26, National Science Foundation.
- Press, W. H., 2007. *Numerical Recipes* 3rd edn, The art of scientific computing, Cambridge Univ. Press.
- Rawlinson, N. & Sambridge, M., 2005. The fast marching method: an effective tool for tomographic imaging and tracking multiple phases in complex layered media, *Explor. Geophys.*, **36**(4), 341.
- Ribeiro, A., Kullberg, M., Kullberg, J., Manuppella, G. & Phipps, S., 1990. A review of Alpine tectonics in Portugal: foreland detachment in basement and cover rocks, *Tectonophysics*, **184**, 357–366.
- Ribeiro, A., Munhá, J., Mateus, A., Fonseca, P., Pereira, E., Noronha, F., Romão, J., Rodrigues, J., Castro, P., Meireles, C. & Ferreira, N., 2009. Mechanics of thick-skinned Variscan overprinting of Cadomian basement (Iberian Variscides), *Comptes Rendus Geoscience*, **341**(), 127–139.
- Ribeiro, A., Munhá, J., Dias, R., Mateus, A., Pereira, E., Ribeiro, L., Fonseca, P., Araújo, A., Oliveira, T., Romão, J., Chaminé, H., Coke, C. & Pedro, J., 2007. Geodynamic evolution of the SW Europe Variscides, *Tectonics*, **26**(6)TC6009, doi:10.1029/2006TC002058.
- Saito, M., 1988. DISPER80: a subroutine package for the calculation of seismic normal-mode solutions, in *Seismological Algorithms—computational methods and computer programs*, pp 469, ed Doornbos, D.J., Academic Press
- San Fernando Royal Naval Observatory (ROA), Universidad Complutense De Madrid (UCM), Helmholtz-Zentrum Potsdam Deutsches GeoForschungsZentrum (GFZ), Universidade De Evora (UEVORA Portugal), Institute Scientifique Of RABAT (ISRABAT Morocco), 1996. The Western Mediterranean BB seismic Network, Deutsches GeoForschungsZentrum GFZ. doi:10.14470/JZ581150.
- Schimmel, M. & Gallart, J., 2007. Frequency-dependent phase coherence for noise suppression in seismic array data, *J. geophys. Res.*, **112**(B4), doi:10.1029/2006JB004680.
- Schimmel, M. & Paulssen, H., 1997. Noise reduction and detection of weak, coherent signals through phase-weighted stacks, *Geophys. J. Int.*, **130**(2), 497–505.
- Schimmel, M., Stutzmann, E. & Gallart, J., 2011. Using instantaneous phase coherence for signal extraction from ambient noise data at a local to a global scale, *Geophys. J. Int.*, **184**, 494–506.
- Schimmel, M., Stutzmann, E. & Ventosa, S., 2017. Measuring Group velocity in seismic noise correlation studies based on phase coherence and resampling strategies, *IEEE Trans. Geosci. Remote Sens.*, **55**(4), 1928–1935.
- Schimmel, M., Stutzmann, E. & Ventosa, S., 2018. Low-frequency ambient noise autocorrelations: waveforms and normal modes, *Seismol. Res. Lett.*, **89**(4), 1488–1496.
- Sebai, A., Stutzmann, E., Montagner, J. P., Sicilia, D. & Beucler, E., 2006. Anisotropic structure of the African upper mantle from Rayleigh and Love wave tomography, *Phys. Earth planet. Inter.*, **155**(1–2), 48–62.
- Silveira, G., Afonso Dias, N. & Villaseñor, A., 2013. Seismic imaging of the western Iberian crust using ambient noise: boundaries and internal structure of the Iberian Massif, *Tectonophysics*, **589**, 186–194.
- Simancas, J.F., Ayarza, P., Azor, A., Carbonell, R., Martínez Poyatos, D., Pérez-Estaún, A. & González Lodeiro, F., 2013. A seismic geotraverse across the Iberian Variscides: orogenic shortening, collisional magmatism, and orocline development, *Tectonics*, **32**, 1–16.
- Simancas, J.F., Poyatos, D.M., Expósito, I., Azor, A. & Lodeiro, F.G., 2001. The structure of a major suture zone in the SW Iberian Massif: the Ossa-Morena/Central Iberian contact, *Tectonophysics*, **332**, 295–308.
- Sousa Moreira, V., Prodehl, C., Mueller, S. & Mendes, A.S., 1983. Crustal structure of western Portugal, in *Developments in Solid Earth Geophysics*, pp. 529–532, eds Bisztricsány, E. & Szeidovitz, G.Y., Elsevier.
- Stockwell, R.G., Mansinha, L. & Lowe, R.P., 1996. Localization of the complex spectrum: the S-transform, *IEEE Trans. Signal Process.*, **44**, 998–1001.
- Tarantola, A. & Valette, B., 1982. Generalized nonlinear inverse problems solved using the least squares criterion, *Rev. Geophys.*, **20**(2), 219–232.
- Téllez, J., Matias, L.M., Córdoba, D. & Mendes-Victor, L.A., 1993. Structure of the crust in the schistose domain of Galicia-Tras-os-Montes (NW Iberian Peninsula), *Tectonophysics*, **221**, 81–93.
- Veludo, I., Dias, N. A., Fonseca, P. E., Matias, L., Carrilho, F., Haberland, C. & Villaseñor, A., 2017. Crustal seismic structure beneath Portugal and southern Galicia (Western Iberia) and the role of Variscan inheritance, *Tectonophysics*, **717**, 645–664.
- Victor, L.A.M., Hirn, A. & VEINANTE, J., 1980. A seismic section across the Tagus Valley, Portugal—possible evolution of the crust, *Ann. Geophys.*, **36**, 469–476.

Wessel, P., Smith, W. H. F., Scharroo, R., Luis, J. F. & Wobbe, F., 2013. Generic Mapping Tools: improved version released, *EOS, Trans. Am. geophys. Un.*, **94**, 409–410.

SUPPORTING INFORMATION

Supplementary data are available at [GJI](https://doi.org/10.1093/gji/ggab028) online.

Figure S1. Example of the energy diagrams obtained by *S*-transform analysis for the station pair PBGR–PFVI, with an interstation distance of 549 km. The colour code corresponds to the signal energy as a function of group velocity and frequency, normalized for each frequency. Red corresponds to high energy, and blue means no energy. The central dot-line indicates the fundamental-mode Rayleigh-wave group velocities. The black dashed lines correspond to the 95 per cent confidence interval. We can clearly identify the group-velocity curve of the fundamental-mode Rayleigh wave. The average group velocity is plotted as a dashed white line for comparison.

Figure S2. Same as Fig. S1 for the station pair PAZA–PW7, with an interstation distance of 240 km. This measurement was considered an outlier as one cannot follow a continuous group velocity as a function of frequency. The average group velocity is plotted in a dashed white line for comparison.

Figure S3. The number of ray paths used in the ambient noise tomography as a function of the period (left) and the interstation distance (right).

Figure S4. Checkerboard test for the periods of 20 s using the fast marching surface tomography (FMST) method (Rawlinson & Sambridge 2005). We present on the left the paths used in the test to guarantee better visibility of the input and retrieved model. We included only ray paths used in the inversion. We present the seismic station locations with coloured triangles using the same

colour code of Fig. 2. The input model, with 50.0 km × 50.0 km anomalies, is shown in the middle. It has a maximum perturbation of velocity nodes of 3.0 km s⁻¹. We added Gaussian noise to the synthetic data with a standard deviation of 0.15 s to simulate the existent noise in measured group velocities. The figure on the right shows the recovered group-velocity model. Seismic stations are all represented with white squares in the middle and right figures. The main differences between the input and the retrieved anomalies occur at the outer limits of the network. Also, some anomalies are smeared in the northwest and southeast Portugal.

Figure S5. Rayleigh-wave group-velocity lateral variations maps for 10, 19 and 29 s. Group-velocity perturbations from average velocity in per cent are displayed by colour coding and vary from -10% to +10%.

Figure S6. Group-velocity sensitivity kernels for four different periods. The V_s model is taken from the inverted 3-D model at 8°W 40.25°N. The computed group-velocity sensitivity kernels show that we can safely discuss the inverted model until the depth of 60 km.

Figure S7. 1-D models of the different tectonic units and corresponding characteristic dispersion curves. GTMZ, Galicia Trás-os-Montes Zone; CIZ, Central Iberian Zone; OMZ, Ossa morena Zone; SPZ, South Portuguese Zone; LTSB, Lower-Tagus and Sado Basins; LB, Lusitanian Basin; AB, Algarve Basin.

Table S1. Parameters used in the inversion. L_{corr} : correlation length; σ_{velocity} : *a priori* error on group velocity.

Please note: Oxford University Press is not responsible for the content or functionality of any supporting materials supplied by the authors. Any queries (other than missing material) should be directed to the corresponding author for the paper.